High-Speed Evanescently-Coupled Waveguide Type-II MUTC Photodiodes for Zero-Bias Operation

Fengxin Yu, Keye Sun, Qianhuan Yu, and Andreas Beling

Abstract—We demonstrate evanescently-coupled $GaAs_{0.5}Sb_{0.5}$/ $In_{0.53}Al_yGa_{0.47-y}As$ modified uni-traveling carrier (MUTC) waveguide photodiodes (PDs) with high bandwidth (BW) of 66 GHz at zero bias and over 100 GHz bandwidth under low bias condition. An $In_xAl_yGa_{1-x-y}As$ dual-integrated waveguide-drift layer which can facilitate efficient light coupling from the waveguide into the absorber over a short length is utilized. A 7-μm long waveguide PD has an internal responsivity of 0.48 A/W at 1550 nm and clearly open eye diagrams at 40 Gb/s are demonstrated at zero bias.

Index Terms—Low power consumption, MUTC, optical receivers, optoelectric devices, photodiodes, zero-bias.

I. INTRODUCTION

HIGH-SPEED photodiodes (PDs) are key components in digital and emerging photonically-driven radio frequency (RF) and millimeter-wave wireless communication systems [1], [2]. Photodiodes that can be operated at zero bias are particularly beneficial since they require no power supply and alleviate the electrical cross-talk that occurs with tight metal wiring in dense photonic integrated circuits and PD arrays [3]. Moreover, zero-bias photodiodes have smaller footprint since they do not have bulky bias circuits, which eases packaging and system design. Previously, we have demonstrated a high-speed and high-power evanescently coupled waveguide integrated modified uni-traveling- carrier (MUTC) photodiode with 105 GHz bandwidth at -3 V [4]. However, at low or zero bias, a bandwidth limitation often arises from discontinuities in the band diagram which can impede carrier transport in these heterojunction PDs [5]. To avoid the potential barrier in the conduction band between the absorber and the wide-bandgap drift layer in an uni-traveling carrier (UTC) PD at low bias, a staggered band lineup (type-II) is beneficial [6]. Such a type-II $GaAs_{0.5}Sb_{0.5}$/InP photodiode with 170 GHz bandwidth at zero bias was demonstrated by Jhih-Min, *et al.*, in 2017 [7]. However, surface-normal illuminated high-speed PDs usually sacrifice responsivity owing to their thin absorber thickness. To achieve high speed and high efficiency simultaneously at zero bias, in this paper, we present an evanescently coupled waveguide type-II MUTC PD with
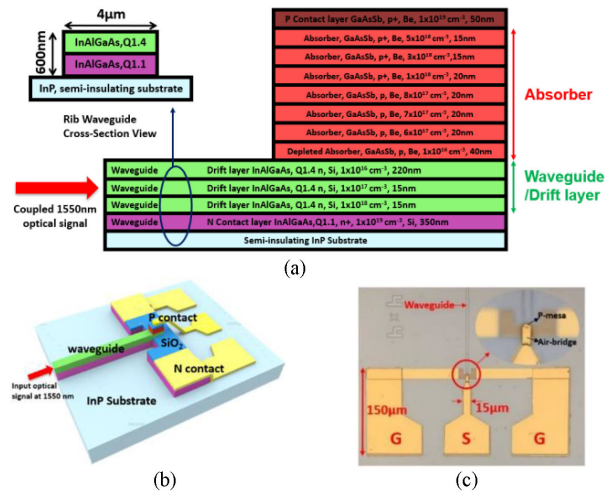
Fig. 1. (a) Epitaxial layers of zero bias waveguide PD. All layers are lattice-matched to InP. Illustration (b) and micrograph (c) of the zero bias waveguide PD.

dual-integrated waveguide-depletion layer. A 3-dB bandwidth of 66 GHz under zero-bias operation and 102 GHz bandwidth at −1 V have been measured for PDs with an active area of $4 \times 4 \ \mu m^2$. Larger PDs ($5 \times 7 \ \mu m^2$) have 56 GHz bandwidth and an internal responsivity of 0.48 A/W at 0 V.

II. DEVICE DESIGN AND FABRICATION

Evanescently coupled waveguide type-II MUTC PDs were fabricated on a $GaAs_{0.5}Sb_{0.5}$/ $In_xAl_yGa_{1-x-y}As$ wafer. The epitaxial layer structure of the wafer, shown in Figure 1(a), was grown on semi-insulating InP substrate by molecular-beam epitaxy and in situ-doped with beryllium (p-type) and silicon (n-type) dopants [8]. The epitaxial layer design consists of two primary parts: a narrow-bandgap $GaAs_{0.5}Sb_{0.5}$ absorber layer and an $In_xAl_yGa_{1-x-y}As$ waveguide-drift layer. Fig 2(a) and 2(b) show the simulated band diagram and electric field distribution inside the absorption and drift layer for the demonstrated device structure under zero-bias using a commercial software (AP-SYS). A 350 nm–thick heavily n-doped $In_{0.53}Al_{0.25}Ga_{0.22}As$ n-contact layer (purple) was first deposited followed by the 250 nm $In_{0.53}Al_{0.09}Ga_{0.38}As$ waveguide-drift layer (green) with graded doping profile ($1 \times 10^{16} \ cm^{-3} - 1 \times 10^{18} \ cm^{-3}$) to provide sufficiently large field under zero-bias (over 10 kV/cm under $1 \ mW/\mu m^2$ light illumination) for high electron velocity which is shown in Figure 2(b). A low background carrier concentration
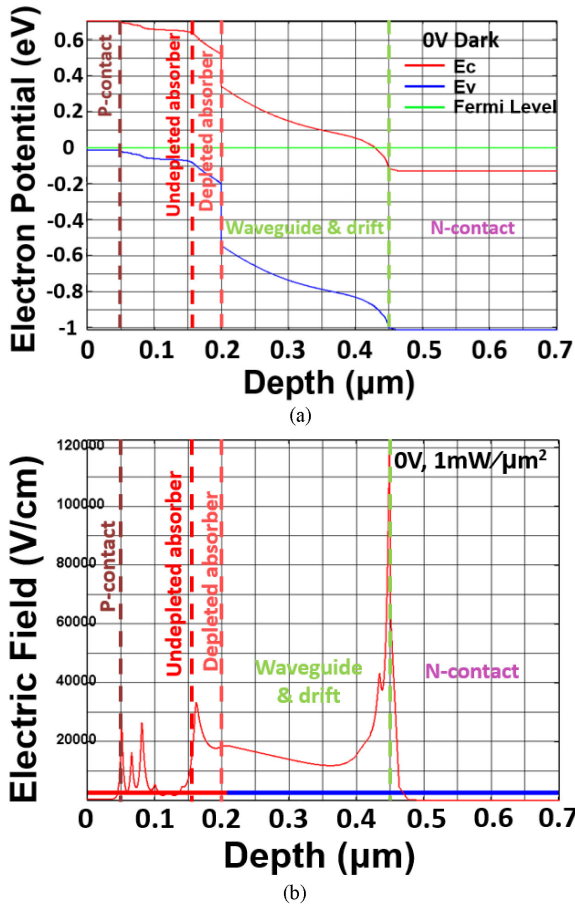
Fig. 2.   (a) Simulated band diagram at 0 V. (b) Simulated electric field distribution at 0 V and 10 mW/μm^2 light illumination at 1550 nm.

Fig. 3.   Dark current versus bias voltage.

Fig. 4.   Measured capacitance versus bias voltage.

in the drift layer is a key aspect for achieving a steep band slope (Figure 2(a)) and a uniform internal electric field distribution (Figure 2(b)) in the drift layer, which can enable high-speed carrier transport at zero bias [9]. In our design the core layer of the passive feeding rib waveguide serves simultaneously as the electron drift layer in the PD. This architecture facilitates light coupling from the waveguide into the adjacent absorber over a short length and thus increases the responsivity [10]. To ensure that the optical mode is mostly confined in regions with low doping, the waveguide-drift layer has a higher refractive index than the underlying highly doped n-contact layer resulting in a confinement factor of 0.6 in the waveguide. Then, for high bandwidth at zero bias, we adopted 150 nm-thick graded doped (5×10^{18} cm^{-3}–1×10^{16} cm^{-3}) GaAs$_{0.5}$Sb$_{0.5}$ as absorber layer which results in type II band alignment at the interface to the In$_{0.53}$Al$_{0.09}$Ga$_{0.38}$As drift layer (shown in Fig 2(a)) and a built-in electric field for electron acceleration (shown in Fig 2(b)). Finally, the p-type contact was formed using 50 nm heavily p-type doped (5×10^{19} cm^{-3}) GaAs$_{0.5}$Sb$_{0.5}$.

Fig. 1(b) shows a schematic of the waveguide photodiode with the electrode configuration. The waveguide PDs were fabricated by using a double-mesa etching process. The first etch was to define the p-mesa and the 4 μm-wide rib waveguide. Then, a second dry etching process was adopted to remove the GaAs$_{0.5}$Sb$_{0.5}$ on
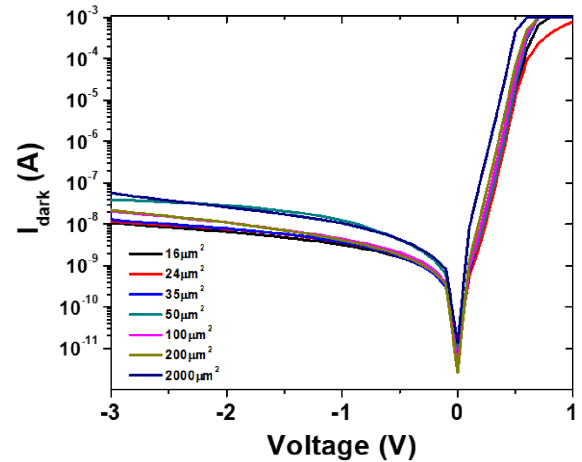
top of the In$_{0.53}$Al$_{0.09}$Ga$_{0.38}$As waveguide rib and to form the n-mesa simultaneously. AuGe/Ni/Au and Ti/Pt/Au metal stack were deposited as n-metal and p-metal contacts, respectively. As shown in Fig. 1(b), the PDs were connected to gold-plated coplanar waveguide (CPW) RF pads through an air-bridge. In order to increase the PD bandwidth, we carefully designed the signal (S) and ground (G) conductors' lengths and widths (Fig. 1c), which varied with the size of the mesa to provide inductive peaking. After fabrication, the completed wafer was cleaved to expose the waveguide facets for light input coupling.

III. CHARACTERIZATION

Waveguide PDs with active areas from 16 μm^2 (4 × 4 μm^2) to 2000 μm^2 (20 × 100 μm^2) were fabricated and the dark current versus voltage curves are shown in Fig. 3. All PDs have a low dark current in the range of 10–100 nA at −3 V bias.

We measured the total capacitance C_{total} of different sized PDs by using an LCR meter and the results are shown in Fig. 4. The capacitance depends only slightly on bias between −0.5 V and −2 V which indicates that our PDs are approaching full depletion in this range. Figure 5 shows the measured capacitance
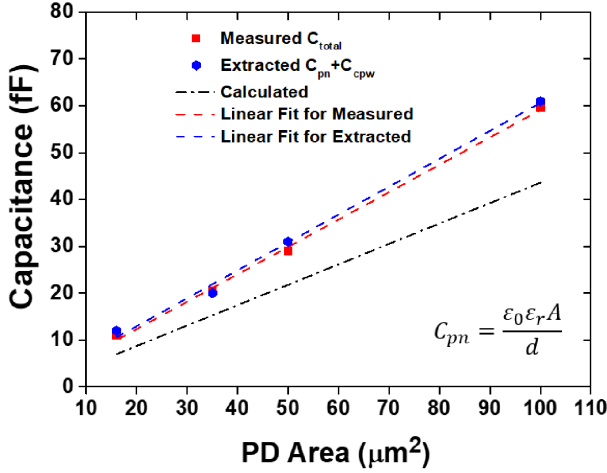
Fig. 5. Measured, extracted from S11 simulation, and calculated capacitance versus PD area at 0 V.

TABLE I
CALCULATED EXTRACTED AND MEASURED PARAMETERS

| PD area (μm^2) | Calculated | Extracted from S11 fitting (0V) | | | | | | CV measurement |
	C_{pn} (fF)	R_d (MΩ)	C_{CPW} (fF)	L_{CPW} (pH)	R_s (Ω)	C_{pn} (fF)	RC BW (GHz)	C_{total} (fF)
16	7	3	4	70	15	8	204	11
35	15	3	6	75	22	14	111	21
50	22	3	7	80	17	24	77	29
100	44	3	9	85	16	52	40	60

Fig. 6. (a) Measured (blue line) and fitted (red line) S11 data for devices with active areas of 16 μm^2 and 35 μm^2. (b) Circuit model of zero-bias PDs for S11 fitting.

TABLE II
RESPONSIVITY SUMMARY

| PD area (μm^2) | Responsivity (A/W) | |
	External R	Internal R
16 (4x4)	0.06	0.17
24 (4x6)	0.08	0.23
35 (5x7)	0.17	0.48

at 0 V, and as expected, a linear relationship between C_{total} and the PD area can be seen. Figure 5 also shows the calculated junction capacitance (C_{pn}), which uses the parallel plate capacitor equation (inset in Fig. 5.), where ε_0, εr, A and d are the permittivity of free space, the dielectric constant (12.7), PD active area, and the depletion width (290 nm), respectively. We attribute the slope difference between measured and calculated capacitance to the additional capacitance that originates from the RF pads (C_{cpw}) and the fact that the PDs are not fully depleted at 0 V. Our results suggest that for a 16 μm^2 waveguide photodiode the capacitance from the RF pads makes up a third of the total capacitance, indicating that the RF pads play a significant role in the RC component of the bandwidth in the smallest photodiode.

The scattering parameter S11 of the PDs was measured up to 67 GHz under zero bias operation by using a vector network analyzer and the results are shown as blue lines in Fig. 6(a). In order to estimate the RC bandwidth of our devices, a simple photodiode equivalent circuit model (Fig. 6(b)) was used to extract the circuit elements through S11 fitting using Advanced Design System (ADS). R_s, R_d, L_{cpw} and R_{load} represent the series resistance, junction resistance, inductance of the CPW pads, and load resistance, respectively. As shown in Fig. 6(a), the fitting curves (red lines) and measured S11 (blue lines) for two PDs with different areas coincide very well on the Smith Charts. Table I summarizes the extracted circuit elements at 0V from ADS, the measured total capacitance, and the calculated C_{pn} and RC bandwidths for different PD active areas. We found a good agreement between the calculated, measured, and extracted
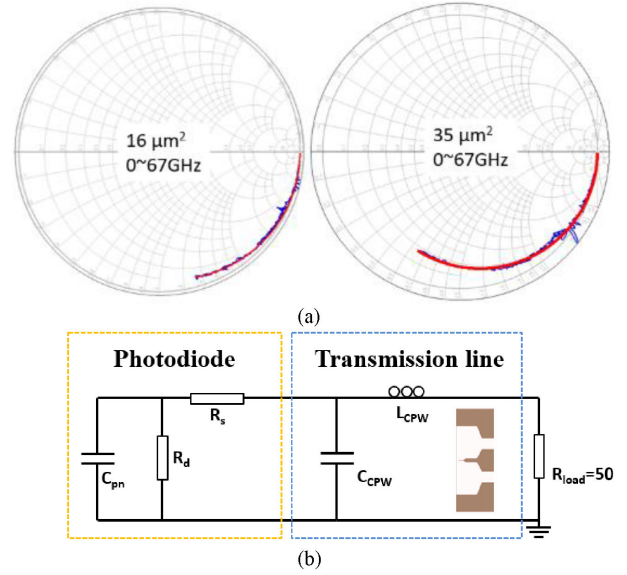
values of the capacitance, which is also shown in Fig. 5. We also found that R_s does not significantly scale with the PD's active area, which indicates a small p-contact resistance and that the bulk resistance dominates. Note that the extracted inductances and capacitance of the CPW pads, L_{cpw} and C_{cpw}, vary with the PD area as the size of the RF pads was optimized for each device.

The responsivities of the waveguide PDs were measured at 1550 nm wavelength under zero bias operation and the results are listed in Table II. The external (fiber-coupled) responsivities were measured using a single-mode tapered optical fiber for input coupling and include the fiber-chip coupling and reflection losses. We expect that the external responsivities can be further increased once we use an anti-reflection coating and reduce the fiber-chip mode-mismatch by, for example, implementing a dual-step coupling scheme similar to the design in ref. [17]. After taking into account the 3 dB fiber-chip mode mismatch loss that was calculated using Beamprop software, and 1.5 dB reflection losses at the waveguide facet, the internal responsivities of waveguide PDs with areas of $4 \times 4 \ \mu m^2$, $4 \times 6 \ \mu m^2$ and $5 \times 7 \ \mu m^2$ are 0.17 A/W, 0.23 A/W, and 0.48 A/W respectively, which indicates that responsivity increases with PD length. Also, since we used a highly doped n-contact layer beneath the waveguide-drift layer, we estimated the losses from free carrier absorption using an
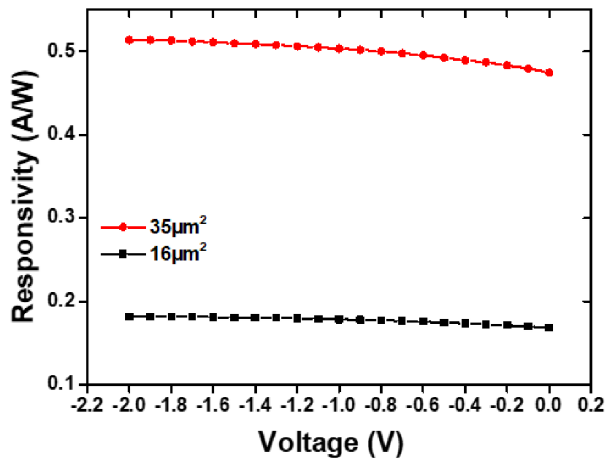
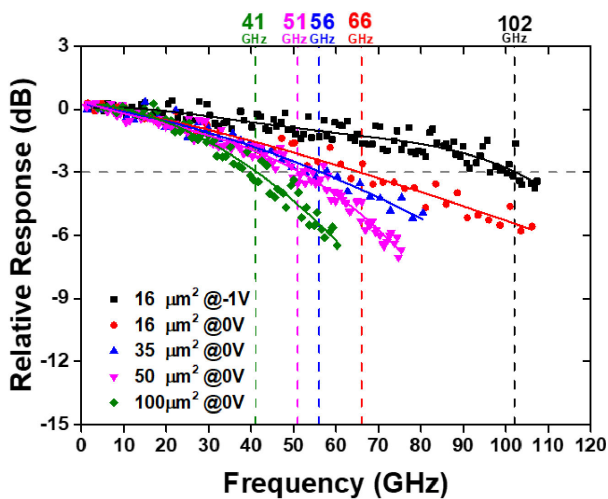Fig. 7. Measured internal responsivity at 1550 nm versus voltage of 16 μm^2 and 35 μm^2 waveguide PDs.

Fig. 9. Measured bandwidth versus reverse bias voltage of 50 μm^2 waveguide PD at 2 mA.

Fig. 8. Frequency responses of waveguide PDs with different PD area at 1mA. (Solid line: polynomial fit)

Fig. 10. Bandwidth at 1550 nm versus reverse bias voltage of waveguide PD with different active area at 2 mA.

absorption coefficient of 0.65 cm^{-1} and Beamprop software. Owing to the small mode overlap with the 1×10^{19} cm^{-3} n-type layer, we found a loss of only 0.1 dB/mm, which indicates that free carrier absorption is not be a main source of waveguide loss. Fig. 7 shows the bias dependence of the internal responsivity for 4×4 μm^2 and 5×7 μm^2 PDs at 1550 nm wavelength. Note that when the voltage changes from 0 V to -2 V the internal responsivity of our waveguide PD has very small variations (0.17 A/W vs. 0.18 A/W and 0.48 A/W vs. 0.51 A/W), which reveals that the built-in electric field is sufficient to collect almost all photogenerated carriers.

An optical heterodyne setup was used to measure bandwidth and saturation characteristics. Light with a wavelength near 1550 nm from two distributed feedback lasers was heterodyned to generate an optical signal with a modulation depth close to 100%. We controlled the frequency of the beat signal by thermally tuning the wavelength of one laser. The RF output power was detected using a calibrated power meter with a frequency range from dc to 1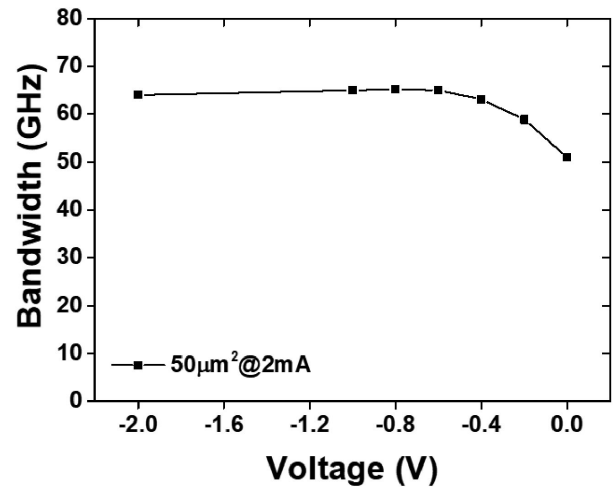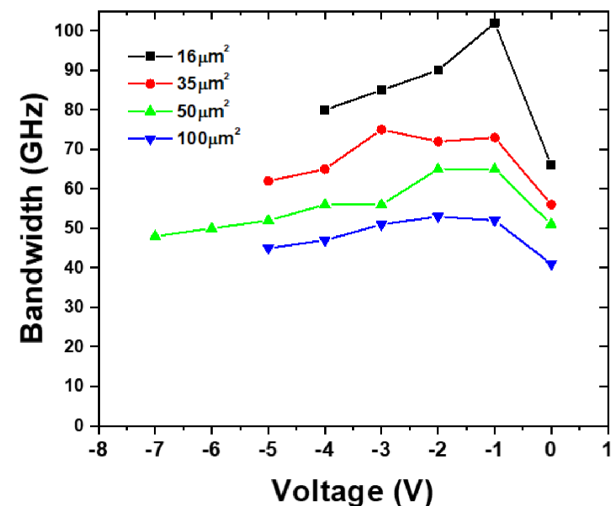10 GHz. Fig. 8 summarize the frequency responses of the devices with various active areas at 1 mA at 0 V and at low bias. At 0 V, waveguide photodiodes with active areas of 16 μm^2, 35 μm^2, 50 μm^2 and 100 μm^2 have bandwidths of 66 GHz, 56 GHz, 51 GHz and 41 GHz, respectively. For the device with an active area of 16 μm^2 a 3-dB bandwidth of 102 GHz was measured when applying -1 V. The bias dependence of the bandwidth for a 50 μm^2 PD at 2 mA is shown in Fig. 9. It is obvious that there is only a small roll-off in bandwidth of 20% below 0.5 V reverse bias, which indicates that the drift layer is nearly depleted under zero bias operation. However, and as shown in Fig. 10, the bandwidths of our devices decrease when applying higher reverse bias (<-1 V). Most likely, the observed bias dependent phenomenon can be attributed to the velocity overshoot of electrons in the drift layer, which has been previously observed in UTC PDs [11], [12]. As shown in Fig. 10, this effect is less pronounced for PDs with large areas since their bandwidth limitation has a larger RC component. For example, the calculated RC bandwidth of a 100 μm^2 PD is
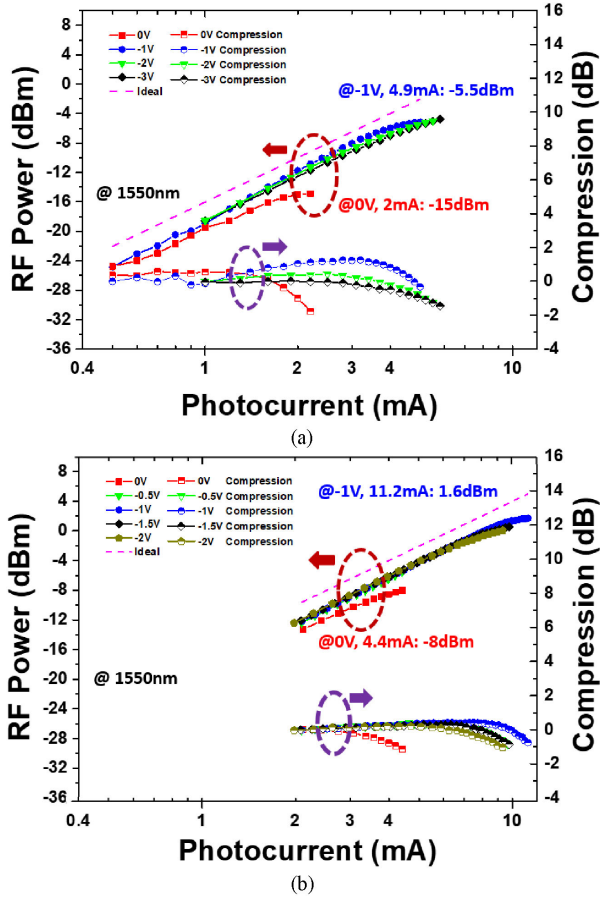
Fig. 11.   RF output power and RF power compression versus photocurrent. (a) $4 \times 4 \ \mu m^2$ at 100 GHz (b) $5 \times 20 \ \mu m^2$ at 40 GHz.

Fig. 12.   (a) Experimental setup for eye diagram measurement. (b) 40 Gbit/s eye diagrams of the $4 \times 4 \ \mu m^2$ and $5 \times 20 \ \mu m^2$ zero-bias waveguide PDs at 0, -1, -2, -3, -4, -5 V. (5 ps/div, 20 mV/div). (EDFA: Erbium-doped fiber amplifier, GSG probe: Ground-Signal-Ground probe).

40 GHz (table I), which is much lower than the estimated transit time limited bandwidth of 120 GHz. For these large-area PDs we expect that a reduction of the doping concentration in the drift layer can ensure full depletion at 0 V which will further increase the RC-component of the bandwidth.

In Fig. 11, the RF saturation was characterized by measuring the RF output power as a function of the average photocurrent at a fixed frequency. Fig. 11(a) and (b) show the RF output power of 16 μm^2 and 100 μm^2 waveguide PDs at 100 GHz and 40 GHz at different voltages, respectively. We found that the power increases super linearly with increasing photocurrent before it saturates. This is the well-known bandwidth enhancement due to the current-induced electric field in the graded absorption layer [13]. In general, as photocurrent increases, the space-charge effect causes an electric field reduction in the depletion region which impedes carrier transport. It ultimately leads to power saturation. We defined the saturation current and power as the photocurrent and power where the RF power compression curve drops by 1 dB from its peak value. When there was no bias, waveguide PDs with 16 μm^2 and 100 μm^2 achieved -15 dBm at 2 mA and -8 dBm at 4.4 mA. At -1 V, the same PDs achieved -5.5 dBm at 4.9 mA and 1.6 dBm at 11.2 mA which can be explained by a reduced space-charge effect. It should be mentioned that the saturation power decreases at higher reverse
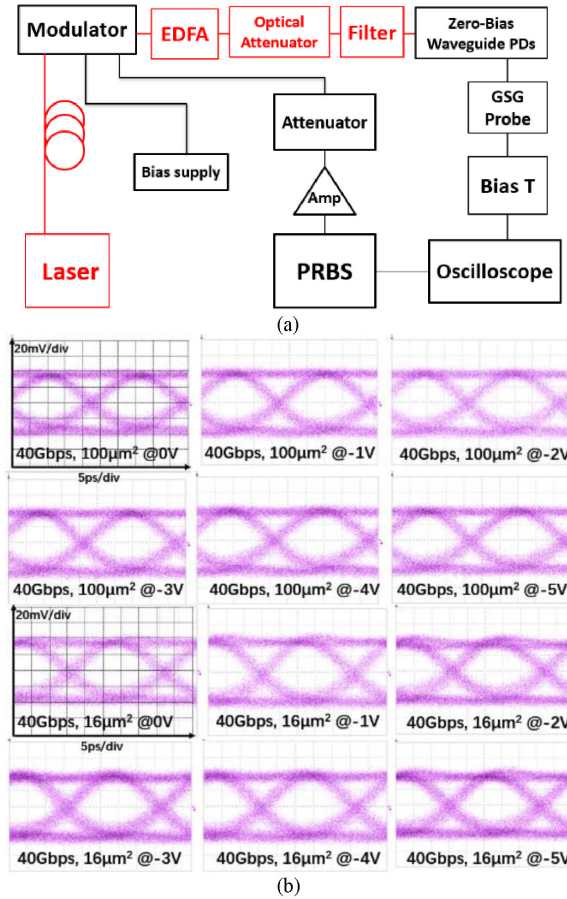
voltages due to the bandwidth reduction shown in Fig. 10. This behavior is in contrast to previous work on high-power waveguide integrated InGaAs/InP MUTC photodiodes which achieved a higher RF output power at high reverse bias [18].

To evaluate our photodiodes for use in high-speed digital optical links we also measured the non-return-zero eye diagrams. Due to equipment limitations in our experiment, the highest available bit rate was 40 Gbit/s. We used a 40 Gbit/s pseudo random binary sequence generator and a 40 GHz Mach-Zehnder (MZ) modulator as the signal source. Fig. 12(a) shows the experimental setup for on-wafer measurements of eye diagrams. By using a commercial 40 Gbit/s LiNbO$_3$ modulator which was driven by a pseudorandom bit sequence (PRBS) generator to modulate 1550 nm light from an external cavity laser (ECL), an optical non-return-to-zero (NRZ) PRBS data pattern at 40 Gbit/s was formed. The PRBS optical signal with pattern length of $2^{31}-1$ was delivered to the waveguide facet of our waveguide PDs. The 40 Gbit/s eye diagrams of the PDs with 16 μm^2 and 100 μm^2 active area at 0, -1, -2, -3, -4, and -5 V are shown in Fig. 12(b). The extinction ratio was 4.8 dB. We observe widely open eye diagrams with a peak voltage of 80 mV at 40 Gbit/s at 0 V, indicating a high-quality data reception performance which is independent of the PD bias.

TABLE III
PERFORMANCE COMPARISON FOR ZERO-BIAS PHOTODIODES

Year	Structure	Type	Measured Responsivity (A/W)	Bandwidth (GHz) @0V	Bandwidth (GHz)	RF Output Power (dBm) @0V	Ref
2015	UTC	Surface Normal	0.14@0V (fiber-coupled)	110	NA	-7@100GHz	9
2015	Germanium PIN	Waveguide	0.84@0V (internal)	40	70@-1V	NA	14
2016	GaAsSb/InP UTC	Surface Normal	0.09@0V (fiber-coupled)	170	170@-1V	-11.3@170GHz	7
2017	Ge-on-SOI PIN	Surface Normal	0.27@0V (fiber-coupled) 0.25@-3V (fiber-coupled)	27	48@-3V	NA	15
2017	InGaAs/InP UTC	Waveguide	0.04@0V (fiber-coupled)	21	35@-1V	-24.1@50GHz	16
2020	**GaAsSb/InAlGaAs MUTC**	**Waveguide**	**0.17@0V (fiber-coupled) 0.48@0V (internal)**	**66**	**102@-1V**	**-15@100GHz**	**This work**

IV. CONCLUSION

In this work, evanescently coupled waveguide type-II GaAs$_{0.5}$Sb$_{0.5}$/In$_{0.53}$Al$_y$Ga$_{0.47-y}$As MUTC photodiodes with high bandwidth and high responsivity at zero bias were successfully demonstrated. At 0 V, the photodiodes achieved 66 GHz bandwidth, 0.48 A/W internal responsivity, and −15 dBm output power at 100 GHz. This performance is among the highest reported for all zero-bias photodiodes (table III) and, to the best of our knowledge, represents a new record for waveguide photodiodes.

ACKNOWLEDGMENT

REFERENCES

[1] T. Nagatsuma, H. Ito, and T. Ishibashi, "High-power RF photodiodes and their applications," *Laser Photon. Rev.*, vol. 3, no. 1-2, pp. 123–137, 2009.

[2] K. Sun and A. Beling, "High-Speed photodetectors for microwave photonics," *Appl. Sci.*, vol. 9, no. 4, pp. 623–638, 2019.

[3] T. Umezawa, K. Akahane, N. Yamamoto, A. Kanno, K. Inagaki, and T. Kawanishi, "Zero-Bias operational ultra-broadband UTC-PD above 110 GHz for high symbol rate PD-Array in high-density photonic integration," in *Proc. Opt. Fiber Commun. Conf.*, 2015, pp. 1–3.

[4] Q. Li *et al.*, "High-Power evanescently coupled waveguide MUTC photodiode with >105-GHz bandwidth," *J. Lightw. Technol.*, vol. 35, no. 21, pp. 4752–4757, Jan. 2017.

[5] T. Ishibashi *et al.*, "InP/InGaAs uni-traveling-carrier photodiodes," *IEICE Trans. Electron.*, vol. 83, no. 6, pp. 938–949, 2000.

[6] L. Zheng *et al.*, "Demonstration of high-speed staggered lineup GaAsSb-InP unitraveling carrier photodiodes," *IEEE Photon. Technol. Lett.*, vol. 17, no. 3, pp. 651–653, Mar. 2005.

[7] J.-M. Wun, R.-L. Chao, Y.-W. Wang, Y.-H. Chen, and J.-W. Shi, "Type-II GaAs0.5Sb0.5/InP Uni-Traveling carrier photodiodes with sub-terahertz bandwidth and high-power performance under zero-bias operation," *J. Lightw. Technol.*, vol. 35, no. 4, pp. 711–716, Feb. 2017.

[8] F. Yu, K. Sun, Q. Yu, and A. Beling, "Zero-bias high-speed evanescently coupled waveguide Type-II UTC photodiode," in *Proc. Opt. Fiber Commun. Conf.*, 2020, pp. 1–3.

[9] T. Umezawa *et al.*, "Bias-free operational UTC-PD above 110 GHz and its application to high baud rate fixed-fiber communication and W-Band photonic wireless communication," *J. Lightw. Technol.*, vol. 34, no. 13, pp. 3138–3147, Jan. 2016.

[10] B. Tossoun, J. Morgan, and A. Beling, "Ultra-Low capacitance, high-speed integrated waveguide photodiodes on InP," in *Proc. Integr. Photon. Res. Silicon Nanophoton.*, Optical Society of America, 2019, pp. 1–2, Paper IT3A-6.

[11] N. Shimizu, N. Watanabe, T. Furuta, and T. Ishibashi, "InP-InGaAs uni-traveling-carrier photodiode with improved 3-dB bandwidth of over 150 GHz," *IEEE Photon. Technol. Lett.*, vol. 10, no. 3, pp. 412–414, Mar. 1998.

[12] J.-W. Shi, Y.-S. Wu, C.-Y. Wu, P.-H. Chiu, and C.-C. Hong, "High-speed, high-responsivity, and high-power performance of near-ballistic uni-traveling-carrier photodiode at 1.55-/spl mu/m wavelength," *IEEE Photon. Technol. Lett.*, vol. 17, no. 9, pp. 1929–1931, Sep. 2005.

[13] Z. Li, H. Pan, H. Chen, A. Beling, and J. C. Campbell, "High-saturation-current modified uni-traveling-carrier photodiode with cliff layer," *IEEE J. Quantum Electron.*, vol. 46, no. 5, pp. 626–632, May 2010.

[14] S. Lischke *et al.*, "High bandwidth, high responsivity waveguide-coupled germanium p-i-n photodiode," *Opt. Express*, vol. 23, no. 21, Aug. 2015, Art. no. 27213.

[15] Z. Liu *et al.*, "48 GHz high-performance Ge-on-SOI photodetector with zero-bias 40 Gbps grown by selective epitaxial growth," *J. Lightw. Technol.*, vol. 35, no. 24, pp. 5306–5310, Dec. 2017.

[16] S. Sun *et al.*, "Evanescently coupled waveguide InGaAs UTC-PD having an over 21 GHz bandwidth under zero bias," *IEEE Photon. Technol. Lett.*, vol. 29, no. 14, pp. 1155–1158, Jul. 2017.

[17] Y.-S. Wu, J.-W. Shi, P.-H. Chiu, and W. Lin, "High-Performance dual-step evanescently coupled uni-traveling-carrier photodiodes," *IEEE Photon. Technol. Lett.*, vol. 19, no. 20, pp. 1682–1684, Oct. 2007.

[18] G. Zhou *et al.*, "High-Power InP-Based waveguide integrated modified uni-traveling-carrier photodiodes," *J. Lightw. Technol.*, vol. 35, no. 4, pp. 717–721, Feb. 2017.